HHS Public Access

Author manuscript

Exp Eye Res. Author manuscript; available in PMC 2019 April 01.

Published in final edited form as:

Exp Eye Res. 2018 April ; 169: 79–90. doi:10.1016/j.exer.2018.01.025.

The Effects of Graded Intraocular Pressure Challenge on the Optic Nerve Head

Nimesh Patel, **Faith McAllister**, **Laura Pardon**, and **Ronald Harwerth**

University of Houston, College of Optometry, 4901 Calhoun Road, Houston, TX 77204

Abstract

Intraocular pressure (IOP) is an important risk factor for glaucoma, and the response of the ONH and surrounding tissues to elevated IOP are often investigated to better understand pathophysiology. In vivo structure including that of the optic nerve head (ONH) and surrounding tissue of the eye are often assessed using optical coherence tomography (OCT). With advances in OCT technology, both large vessels and capillaries can be imaged non-invasively (OCT Angiography). Because a significant portion of retinal thickness is comprised of vasculature, the purpose of the current study was to investigate OCT structural and vascular changes in healthy non-human primate eyes with systematic graded increases and decreases in IOP. Six healthy animals with no previous experimental intervention were used. The pressure in the anterior chamber was adjusted from 10 mmHg to 60 mmHg and back to 10 mmHg in 10 mmHg steps every 10 minutes. Using optical coherence tomography (OCT), retinal nerve fiber layer (RNFL) thickness, minimum rim width (MRW), Bruch's membrane opening (BMO) size and relative height, anterior lamina cribrosa surface (ALCS) depth, choroidal thickness, and angiography (OCTA) were quantified. With IOP challenge there were significant changes in all morphological measures quantified ($p<0.01$) other than BMO size ($p=0.30$) and RNFL thickness ($p=0.29$). Specifically, the position of the BMO was sensitive to both an increase and decease in IOP. The inner retinal capillary density gradually decreased with increasing IOP, reaching statistical significance when pressure exceeded 50 mmHg, but returned when IOP was reduced. The average choroidal thickness around the ONH decreased for elliptical annuli 500–1000 μm and 1000–1500 μm, from the BMO, with increasing IOP ($p<0.01$). For the 1000–1500 μm annulus, choroid thickness did not return to baseline with IOP reduction. Similarly, the MRW decreased with increase in IOP, but with pressure reduction did not return, and at the final 10 mmHg time point was thinner than at baseline ($p<0.01$). The results from this experiment illustrate differences in ONH neural rim tissue, RNFL and vessel density changes with acute IOP challenge. Overall, vessel collapse could not completely account for changes in RNFL or ONH MRW thickness. The study supports the hypothesis neural rim compression may be an important part of IOP-induced damage.

Corresponding author: Nimesh Patel, npatel@central.uh.edu.

Disclosures: All authors: None

1.0 INTRODUCTION

The glaucomas are progressive optic neuropathies with characteristic losses of visual function and structural alterations in the retina and optic nerve head (ONH). The pathophysiology of glaucoma is not understood completely, but intraocular pressure (IOP) has been identified as an important risk factor in all clinical forms (Anderson, 2003; Gordon et al., 2002; Leske et al., 2004; Quigley and Addicks, 1980). High IOP seems integral to the pathology of glaucoma, and the effects of IOP on posterior segment structures have been studied and modeled in healthy and glaucomatous eyes using both *in vivo* and *ex vivo* preparations.

From early experiments that involved both acute and sustained elevation of IOP in a primate model, the ONH was identified as the primary site for disturbances in axonal transport (Anderson and Hendrickson, 1974; Quigley and Anderson, 1976; Quigley and Anderson, 1977). Subsequently, in enucleated eyes implanted with platinum wire, displacement of the lamina was shown with increase in IOP (Levy and Crapps, 1984; Levy et al., 1981). As non-invasive *in vivo* imaging technologies evolved, the ONH and surrounding tissues have been quantified with increasing precision and accuracy, and the effects of acute changes in IOP on load bearing structures of the posterior segment investigated in healthy and disease eyes (Burgoyne et al., 1995; Burgoyne et al., 1994; Fortune et al., 2009; Heickell et al., 2001; Ivers et al., 2016; Morgan et al., 2002; Quigley and Pease, 1996; Sharma et al., 2017; Strouthidis et al., 2011). These studies, along with histological evidence, have identified the peripapillary connective tissue, lamina cribrosa, and neural tissue as structures susceptible to IOP related stress (Burgoyne, 2011; Downs, 2015; Sigal et al., 2014).

Because OCT based peripapillary retinal nerve fiber layer (RNFL) thickness and ONH neural rim tissue measures, sample a majority of the retinal ganglion cell (RGC) axons, they are commonly used for the clinical diagnosis and management of glaucoma patients. In principle glaucomatous RGC axonal loss should result in proportional losses of the two measures, but ONH neural retinal rim measures have been shown to thin prior to RNFL in both longitudinal and cross sectional studies (Fortune et al., 2013; He et al., 2014; Patel et al., 2014). The discrepancy between ONH neural rim tissue thinning and that of RNFL could be due to differences in axonal characteristics, glial tissue, extracellular matrix or vasculature.

Recent advances in optical coherence tomography (OCT) imaging allow for non-dye based angiography (OCTA) of the major retinal vasculature and capillary networks. Using OCTA technology a decrease in peripapillary vascular density in both glaucoma patients and glaucoma suspects has been shown (Akil et al., 2017; Chen et al., 2016; Lee et al., 2016, 2017; Rao et al., 2016; Suh et al., 2016; Yarmohammadi et al., 2016). Although OCTA does not directly quantify flow, it provides useful insight to when blood flow has reduced beyond the capability of OCTA algorithms to detect.

The non-human primate has similar structure to that of humans, with similar relationships between ONH neural rim tissue and RNFL thickness (Patel et al., 2014), hence ideal for investigations of structural change with IOP and experimental glaucoma. IOP in this

experimental model often ranges between 25–45mmHg, and at these moderate to high IOPs, it is possible that capillary networks can be compressed adding variability to studies investigating rates of change in nerve fiber layer and capillary densities. However, changes in OCTA based peripapillary and ONH capillary density with IOP challenge remains unknown in primate eyes. Hence, the purpose of the present study was to quantify both structural and vascular changes, and the relationship between the two, in healthy non-human primate eyes with systematic, controlled graded increase and return in IOP. Some of the results of these studies have been presented in abstract form (Patel NB, et al. ISER/BrightFocus Glaucoma Symposium 2017).

2.0 METHODS

2.1 Subjects

A total of six (five males and one female) rhesus monkeys (*Macaca mulatta*) with an average age of 5.2 yrs were subjects in the study (Table 1). One randomly selected healthy eye of each animal, with no prior experimental manipulation, was used for data collection and analysis (4 right eyes and 2 left eyes). In addition to the cannulation experiment, each animal was re-evaluated at least two weeks after the initial experiment to assess overall ocular health. Experimental and animal care procedures were reviewed and approved by the Institutional Animal Care and Use Committee of the University of Houston. The use of animals for these experiments confirmed to National Institutes of Health guidelines for the care and use of laboratory animals.

2.2 Animal Preparation

Animals were anesthetized with an intramuscular injection of ketamine (20–25 mg/kg/hr) and xylazine (0.8–0.9 mg/kg/hr), administered at hourly intervals, and treated with a subcutaneous injection of atropine sulfate (0.04 mg/kg). Atropine sulfate was re-administered if the heart rate fell below 75 beats per minute, at a dose of 0.02 mg/kg. Throughout the experiment, body temperature was monitored and maintained at 37° Celsius using a thermal blanket (TC 1000 temperature controller CWE, Ardmore, PA). Heart rate and pulse were monitored continuously using a pulse oximeter, while blood pressure was monitored every 5 minutes using an automated inflatable cuff (petMAP+II, Ramsey Medical, Tampa, FL). The animal's pupils were dilated with 1% tropicamide. To prevent infection, 5% ophthalmic betadine (Alcon Laboratories, Fort Worth, TX) was applied to the eyelids, instilled on the ocular surface, and subsequently washed off with sterile balanced salt solution (BSS, Alcon Laboratories, Fort Worth, TX) after a period of two minutes. The head of the animal was stabilized using mouth and occipital bars. A sterile eyelid speculum was used to keep the eye open, and a plano power rigid gas permeable contact lens was placed on the eye to prevent corneal dehydration and maintain optical clarity throughout the experiment. Following anterior chamber cannulation and completion of data collection, the contact lens and needle were removed, and topical antibiotics (polymyxin B/trimethoprim and moxifloxacin) were instilled on the eye.

2.3 IOP Control

The anterior chamber was accessed using a 27G butterfly needle, inserted approximately 0.5 – 1 mm from the temporal limbus and extending up to 2 mm into the anterior chamber. The needle was connected to a pressure control system with sterile microtubing filled with BSS. The pressure control system (Fig 1) included a capacitive pressure transmitter (Keller PR-41X, Keller America, Newport News, VA) coupled with a syringe pump (Cole-Parmer, Vernon Hills, IL) that was monitored through a MATLAB (The Mathworks, Natick, MA) program (5Hz sampling). To ensure accurate pressure control, the pressure sensor and syringe pump were adjusted to the same height as the cannulated eye. For this experiment, the initial IOP was set at 10 mmHg, and the eye was scanned after a 10 minute duration at this pressure. Subsequently, the IOP was increased to 20 mmHg, and the eye was scanned again after 10 minutes. This increase in pressure by 10 mmHg and scanning pattern was continued up to 60 mmHg, after which the IOP was decreased in 10 mmHg steps to the baseline of 10 mmHg. At each setting, the eye was scanned after pressure had stabilized for the 10 minutes.

2.4 Optical Coherence Tomography

All OCT scans were acquired using beta version software (SP-X1601), on the Spectralis OCT2 system (Heidelberg Engineering, Heidelberg, Germany). Prior to scan acquisition at each pressure setting, a 20° vertical and horizontal section through the ONH was used to align the optics of the system to minimize tilt of the b-scan. Two scan protocols were used for ONH quantification, and all scans in each series were acquired using the auto-rescan feature to minimize noise in measurement from variable centration. For ONH structural analysis, a 24-line, 20° radial scan centered on the ONH, with averaging of 20 frames, was acquired. The OCTA protocol included a 15×15°, 391-line raster scan, with averaging set at 30 frames, centered on the ONH. Prior to analysis and data export, all scans were excluded from follow-up progression to minimize artifacts from auto-alignment of scans. Although structural data were exported as *.vol files, these don’t contain angiography information, which were saved as *.tif images.

2.5 Ocular Biometry and Transverse Retinal Scaling

Prior to needle placement, ocular biometry, including corneal curvature, anterior chamber depth, lens thickness, and axial length, were obtained using an optical biometer (Lenstar LS900, Haag-Streit, Koeniz, Switzerland). Crystalline lens curvature was interpolated from normative data (Qiao-Grider et al., 2007). These parameters were used to compute individualized, three-surface schematic eyes, and the transverse retinal scaling (μm/deg) was calculated from the second nodal point to the retina. Additional details on scaling have been described previously (Patel et al., 2017; Patel et al., 2011; Patel et al., 2014).

2.6 ONH and Choroid Analysis

Radial B-scans were exported as raw (*.vol) files, imported into MATLAB, and scaled to a 1:1 aspect ratio using the computed transverse scaling (Fig. 2E). Files were randomized such that trained observers (FM and LP) analyzing the scans were not aware of the pressure at which they were obtained. Borders of the inner limiting membrane (ILM) and Bruch’s

membrane (BM) were manually corrected for segmentation errors. The choroid/sclera border was manually segmented after each B-scan was compensated/enhanced (Girard et al., 2011). The compensated images were also used to manually identify the anterior lamina surface, and only for portions of the scan where this surface was visible. Subsequently, the location and dimension of the Bruch's membrane opening (BMO) was determined by marking the two corresponding locations on each radial B-scan. Specifically, BMO area was quantified using a best-fit ellipse to the marked points. BMO height was calculated as the perpendicular distance from the BMO points to a reference defined by the best fit plane to points 2mm from the center of the BMO aligned to the BM (i.e. 2 mm radius circular plane, Fig. 3). To quantify anterior lamina cribrosa surface (ALCS) depth, a thin plate spline was first fit to the lamina points to estimate the surface within the BMO region, assuming no focal regions of loss between sampled scans or in areas under major vessel shadows. The average perpendicular distance from a plane fit the BMO points to the ALCS thin plate spline fit was used to calculate the BMO-ALCS depth. Because greater change in ALCS position has been previously reported using a more distal reference (Strouthidis et al., 2011), the ALCS position was also quantified using a 4 mm diameter reference plane centered on the BMO and aligned to the choroid/sclera junction (Sclera-ALCS). The minimum neuroretinal rim width (MRW) was quantified as the shortest distance from the BMO opening to the ILM on each radial b-scan, and average MRW was used for analysis. Choroid thickness was determined using the BM to choroid/sclera segmentation. A thickness map using these data was generated using linear interpolation, and subsequently average thickness for annular bands at eccentricities corresponding to; 1) BMO to 500 μm, 2) 500 μm to 1000 μm from the BMO, and 3) 1000 μm to 1500 μm from the BMO, were quantified (Fig 2D).

2.7 Retinal Nerve Fiber Layer Analysis

For peripapillary RNFL quantification, an elliptical scan path 550 μm from the BMO was interpolated from the 15×15°, 391-line raster scan acquired for OCT angiography (Fig. 2A&B). This distance was selected based on previous work, which showed this eccentricity to be best related to the standard circular scan, and accounted for the elliptical nature of the ONH (Patel et al., 2011). In brief, the locations of BMO points on the radial scan scanning laser ophthalmoscope (SLO) image were registered (i2k retina, DualAlign LLC, Clifton, NY) to the raster scan, from which a 550 μm-eccentricity scan path was used to interpolate a B-scan 1536×496 pixels in dimension. Using these methods, the initial 10mmHg scan data for each subject were used to determine the baseline scan path location, which was subsequently transferred through image registration to all raster scans for that subject. Although the first scan was not randomized, all subsequent scans in the series were analyzed in random order. A custom algorithm was used to segment the RNFL, and segmentation errors that were most common around major vessels were manually corrected by a trained observer (NP). Using the raster scan SLO image and B-scan shadows as a guide, the borders of each major vessel were marked, and the circular region corresponding to each vessel was subsequently subtracted from the RNFL thickness. Specifics for the scan interpolation and segmentation methodology have been presented previously (Patel et al., 2011; Patel et al., 2014).

2.8 OCT Angiography

OCT angiography scans were acquired using beta version software (SP-X1601) on the Spectralis OCT2 system. The research module uses decorrelation-based algorithms to identify motion within the tissue based on acquisition of consecutive B-scans. A 150 μm-thick slab referenced to the ILM was projected, exported as tag image file format (TIFF) images, contrast adjusted (0 to 255), and used for analysis. Thereafter, using a Frangi filter (Frangi et al., 1998), vessels were accentuated and subsequently binarized using Otsu's thresholding (Fig 4). Vascular density was quantified as a ratio of white to black pixels in three annular zones; 1) within the BMO, 2) BMO to 500 μm, and 3) 500 to 1000 μm (Fig. 4D). For the most, the annulus corresponding to BMO to 500 μm included vessels from the superficial vascular plexus, while the outer annulus also included vessels in the deep vascular plexus.

2.9 Statistical Analysis

For each retinal or ONH parameter, global/average measures were computed and used for comparison. A one-way repeated measures ANOVA was used to determine statistical differences for each measure as a function of IOP. When significant ($p<0.01$), parameters for increasing IOPs were compared to the baseline value at 10 mmHg, while for decreasing IOPs, measures were compared to those at 60 mmHg in order to assess recovery. Additionally, to determine if each metric had returned to baseline, the initial and final scans at an IOP of 10 mmHg were compared. To account for multiple comparisons, Sidak correction was applied. Linear regression methods were used to compare relationships between structural and vascular density measures, and for similar metrics quantified at varying eccentricities. All statistical analyses were performed in GraphPad Prism 7 (GraphPad Software, Inc, La Jolla, CA). To illustrate morphological change, the average difference (± standard error) from the 10 mmHg measure was plotted (Fig 5&6) using SigmaPlot 13.0 (Systat Software, Inc, San Jose, CA).

3.0 RESULTS

Each of the six monkeys in this study maintained good systemic and eye health during the experimental session and subsequent recovery period. Subject age, biometry and range of mean arterial pressure are listed in Table 1. Individual mean arterial pressures at each IOP setting are presented in the supplemental table. Data for the means, standard deviations, and repeated measures ANOVA of each parameter quantified are illustrated in Table 2.

3.1 RNFL thickness

The mean peripapillary RNFL thickness with major retinal vascular removed, for a scan path 550 μm from the BMO was 114.27 μm ± 5.12 μm at the initial 10 mmHg pressure setting. With transient increase in IOP, RNFL thickness reduced by 1.56 ± 1.26 μm at 60 mmHg IOP (Fig. 5A), but was not statistically significant ($p=0.21$). Similarly, there was no change in the major vascular contribution to the RNFL comparing baseline 10 mmHg contribution (12.68%) to that at 60 mmHg (12.74%, $p>0.9$). At the follow-up scan session, RNFL thickness (115.12 ± 5.28 μm) was not statistically different than that quantified at the initial 10 mmHg time point ($p=0.93$).

3.2 ONH morphology

Of the five ONH parameters analyzed, three, i.e., MRW (Fig. 5B), BMO height (Fig. 5D), and Sclera-ALCS (Fig. 5F), demonstrated statistically significant change with short-term IOP challenge, while two, i.e., BMO opening size (Fig. 5C), and BMO-ALCS (Fig. 5E) did not. On average, with each incremental increase in IOP, there was posterior movement of the BMO height, with approximately the same return towards baseline as IOP was decreased (Fig 5D, $p<0.01$). However, it is important to note that while 4 of the 6 animals showed this incremental change (maximum change = 69 μm), 2 animals only had < 22 μm change and was non-incremental in nature. The BMO height returned towards baseline with decrease in IOP, and at the final 10mmHg scan, extended past that measured at the initial 10 mmHg (mean = 7.7 μm, range = −6.8 – 22.3μm) for all but one animal. However, this overshoot of the BMO position was not statistically significant ($p=0.80$).

The BMO-ALCS depth, did not change with either increase or decrease in IOP ($p=0.21$). However, a greater than 10 μm increase in depth was noted for 3 animals, while 2 showed a decrease of at least 10 μm, and one animal did not have any significant change. In contrast, the Sclera-ALCS, which includes the change in BMO height minus any change in choroid thickness, showed a significant increase in depth with IOP increase that returned to baseline when IOP was returned to 10 mmHg. Unlike BMO height, the average Sclera-ALCS at the final 10 mmHg setting did not extend past that measured at the initial 10 mmHg. Similar to BMO height, there was a non-incremental increase in depth for the same two animals.

There was a statistically significant reduction in the MRW referenced to the BMO ($p<0.01$) with change in IOP (Fig. 5B). As IOP was increased, there was a decrease in MRW with maximum reduction at 60 mmHg (mean difference from baseline = 29.58 ± 8.2 μm, $p<0.01$). However, when IOP was returned towards 10 mmHg, the MRW did not show a significant rebound and was statistically different from measurements at 60 mmHg (maximum mean difference from 60 mmHg = 5.25 μm, $p=0.20$). MRW did, however, return to its initial baseline value at the follow-up scan session (mean difference = −3.8 ± 2.8 μm, $p=0.82$). Hence, these data demonstrate a longer time course for recovery of MRW with lowered IOP than could be determined from these experiments.

3.3 Choroidal Thickness

The IOP effects on choroidal thickness varied with distance from the BMO of the ONH (Table 2, Figs.63A–C). The choroidal thickness in the annular zone from the BMO to an eccentricity of 500 μm (Fig. 6A) showed a mild reduction with IOP increase up to 60 mmHg (mean difference = 6.0 ± 7.6 μm), which rebounded to the 10 mmHg baseline with pressure reduction. Although a statistically significant change was noted on ANOVA, none of the compared measures reached significance (Fig 6A) when multiple comparisons were accounted for. A similar trend was seen for choroidal thickness quantified for the annulus between 500–1000 μm (Fig. 6B, $p<0.01$), however the relative changes in thickness were greater than the BMO-500 μm zone (e.g. at 60mmHg mean difference from 10mmHg = 12.6 ± 6.3μm). In contrast, choroidal thickness in the annular zone between 1000–1500 μm showed larger thickness changes, which were significant for IOP levels greater than 30 mmHg (Fig. 6C, $p<0.01$). For comparison, at 60mmHg, the mean difference from 10mmHg

was 17.3 ± 7.9 μm. Though the choroidal thickness at this location increased during the IOP lowering phase of the challenge, it did not returned to baseline by the 10 mmHg time point (mean difference = 13.8 μm, $p<0.01$).

The average choroid thickness at baseline was greater for the annulus furthest from the BMO and least for that closest to the BMO ($p<0.01$, Table 2). To investigate if the proportion of choroid change was similar for all three annuli, data were normalized to the initial 10mmHg thickness for each annulus, and a percentage change calculated for each pressure step. The percent choroid thickness was related for each of the three annular zones as illustrated in figure 7. However, the slopes of the functions fit to the grouped data were significantly different ($p<0.01$), suggesting a greater percentage change for the BMO-500μm annulus, with decreasing percentage change with increasing eccentricity.

3.4 OCT Angiography

The effect of elevated IOP on OCT angiography, of a 150 μm slab referenced to the ILM, are illustrated for all six subjects in Fig 8, and the quantified vessel density data presented in Figs. 6D–F. Overall, vessel density was greater within the BMO, and decreased with increase eccentricity ($p<0.01$). The vessel density inside the BMO decreased, reaching statistical significance when IOP exceeded 50 mmHg ($p<0.01$, Fig. 6D), and vessel density recovered to baseline when IOP was returned to 10 mmHg. This trend was similar for the annular zones from BMO-500 μm (Fig. 6E, $p<0.01$) and 500–1000 μm (Fig. 6F $p<0.01$). As OCT angiography is dependent on blood flow through vasculature, change in vessel density was also plotted as a function of ocular perfusion pressure (OPP), calculated as (MAP – 7) – IOP (Fig 9). The 7mmHg adjustment to the MAP was to account for the difference in height of where blood pressure was measured and the eye. For a large portion of the OPP range, vessel density was constant. Although there is significant intra and inter subject variability, and a clear breakpoint could not be clearly ascertained for any of the three eccentricities (Fig 9), vessel density, based on a two segment linear fit, only decreased when OPP fell below; 1) 51.0 ± 14 mmHg within the BMO ($p<0.01$), 2) 43.0 ± 7.5 mmHg for the BMO - 500μm annulus ($p<0.01$), and 3) 41.0 ± 6.0 mmHg for 500–1000μm annulus ($p<0.01$).

Because vessel density is a normalized metric, no additional data transformation was performed to compare changes in density in the three regions with IOP. Change in vessel density for the three zones analyzed were linearly related as illustrated in figure 10. The slope of the best fit linear function for the grouped data for each comparison were not significantly different from each other ($p=0.92$), or from 1 (BMO-500 μm as a function of BMO, $p=0.15$, 500–1000 μm as a function of BMO, $p=0.26$, and BMO-500 μm as a function of 500–1000 μm, $p=0.56$).

As vessel compression could result in tissue thinning, the relationship between; 1) BMO vessel density and MRW, and 2) 500–1000 μm vessel density and RNFL thickness was investigated. To compare similar measures, both MRW and RNFL were normalized and expressed as percentage change from baseline measures. Overall, there was no significant relationship between change in vessel density and either MRW ($p=0.07$) or RNFL thickness ($p=0.52$, Fig. 11).

4.0 DISCUSSION

Objective measures of the ONH and surrounding tissues provide important information on assessing optic neuropathies. While the pathophysiology of glaucoma is not yet understood, elevated IOP is a significant, and only modifiable risk factor. The present study was undertaken in order to determine the effects of short-duration graded increases and subsequent reductions of IOP on the ONH and surrounding tissues using OCT imaging in healthy eyes of non-human primates. The principal findings were that several structural and vascular parameters showed IOP-related changes, and in some cases the tissue responses to increased IOP were different from those seen on IOP return. In general, the results of the investigation are important for understanding of the clinical biomarkers of glaucoma, with respect to whether they are affected by the immediate pressure environment during measurement or if they are more reflective of the stage of neuropathy, irrespective of the IOP at the time of assessment.

Among the ONH parameters, the BMO size showed minimal change with acute increase and subsequent return in IOP. This finding is similar to that seen in other *in vivo* imaging studies in human and non-human primate eyes (Jiang et al., 2015; Sharma et al., 2017; Strouthidis et al., 2011). However, it is likely that the BMO size does not reflect directly on underlying collagenous scleral canal opening, which has been shown to expand in ex vivo histological studies in healthy primate eyes with higher set pressures, and for longer durations (Yang et al., 2009).

Although the anterior lamina surface (ALCS) can be visualized with some certainty in non-human primates, the methods used for this study were not sufficient to visualize the posterior surface and hence quantify lamina thickness. As is typical, the ALCS depth was first referenced to the BMO plane, which is separated from the scleral opening by a thin layer of choroid, and didn't change with acute IOP challenge (data not shown, mean thickness BMO-100 μm annulus = 39.3 ± 18.0 μm, p=0.15). On average there was no change in the BMO-ALCS depth with short duration change in pressure, but there was variability in the depth response, with an increase in BMO-ALCS depth noted for half the subjects. This finding is similar to that noted in other human and non-human primate studies (Agoumi et al., 2011; Fazio et al., 2016; Ivers et al., 2016; Strouthidis et al., 2011), and the direction of BMO-ALCS change has been proposed to reflect on the lamina and peripapillary scleral rigidity (Sigal et al., 2011).

With short-duration increases in IOP, there was also a posterior shift in the BMO location, referenced to a 4 mm diameter plane (BMO Height), which then returned towards baseline with IOP. Although there are differences in how images were analyzed, this finding is similar in magnitude to that previously reported in this species for measures stabilized at 10 mmHg for 30 minutes and 45 mmHg for 60 minutes (Strouthidis et al., 2011). In that study, the investigators also showed a decrease in ALCS depth when referenced to a plane 1500 μm from the centroid of the neural canal opening and aligned to the BM. However, when referenced to a plane aligned to the BM, the posterior deflection in ALCS depth with increase in IOP also includes choroidal thickness, which is variable between individuals, has diurnal variation, changes with age, and is known to decrease with increase in IOP

(Johnstone et al., 2014; Song et al., 2016; Wang et al., 2016). In order to mitigate fluctuations in choroidal thickness, when a scleral reference was used, the Sclera-ALCS depth increased with IOP and showed recovery when IOP was returned to 10 mmHg. These findings suggest that in addition to BMO-ALCS, which is known to change with IOP challenge in early glaucoma (Ivers et al., 2016), a scleral reference, which has been proposed by others (Johnstone et al., 2014), and as described in the current work, might also provide useful information.

Peripapillary RNFL thickness and ONH neuroretinal rim (NRR) parameters have been shown to have good correspondence with retrobulbar axon counts, and are often used to assess the retinal ganglion cell (RGC) content of the eye (Cull et al., 2012; Fortune et al., 2016a). In addition, a short-duration stepwise increase and return of IOP should not result in significant loss of RGCs, as is evident from the similar measures for both RNFL and MRW at the initial 10 mmHg time point and at follow-up. Although a statistically significant reduction in RNFL thickness with acute increase in IOP has been reported (Fortune et al., 2009), this was not seen in the present study. However, it is noteworthy that in the previous work, IOP was increased for a longer duration (45 mmHg for 60 min), and a 1.6 μm decrease in RNFL thickness was shown at 1120 μm from the center of the ONH. This reduction is similar to the 1.56 μm reduction observed in the current study at 60 mmHg for elliptical scans 550 μm from the BMO.

In the healthy primate eye approximately 14% of the peripapillary RNFL thickness is from major retinal vasculature (Hood et al., 2008; Patel et al., 2014; Patel et al., 2010), and about 7.5% from peripapillary capillaries (Henkind, 1967; Scoles et al., 2009; Yu et al., 2014). In the current study, short duration increase in IOP did not result in a change in major retinal vascular contribution to the RNFL thickness, as determined on the OCT structural scans (Fig 2B). Although individual vessel diameters were not quantified on OCTA images, the finding on OCT thickness measures correspond to similarities in the major vessel appearance at 10 and 60 mmHg on OCTA images (Fig 8). In contrast, at higher pressures, capillary networks were not clearly visible, as is illustrated by the decrease in vessel density at 60 mmHg. Decrease in capillary density could be a reflection of reduction of flow below detection by the OCTA system, or collapse of the capillaries. While change in vessel density was not related to RNFL thickness, if capillaries have collapsed at higher pressures, a corresponding reduction in RNFL thickness would have also been expected. Specifically, the average reduction of 9.8% vessel density at 60 mmHg should have resulted in about 7.2 μm loss of thickness, based on 7.5% RNFL capillary, and 12.7% constant major retinal vessel contribution. However, loss of capillaries in these experiments does not represent complete loss of a vessel, but likely only lumen collapse. Assuming a lumen size of 5 μm, the walls of an average capillary would have to be 3.4 μm to achieve the observed 1.54 μm change in RNFL thickness. Specifically, in this case, the capillary lumen would constitute 18% of the vessel cross sectional area, corresponding to approximately 1.5 μm average thickness (i.e., 114 μm RNFL x 0.075 capillary contribution x 0.018 vessel lumen size). It is also possible that a decrease is thickness is not seen because of axonal swelling, or the support provided by columnar nature of neural tissue in the retina. To determine the exact response of capillaries to IOP challenge, and their relationship to surrounding axonal bundles, higher resolution adaptive optics imaging is needed (Musial et al., 2017; Scoles et al., 2009).

The ONH NRR measure, MRW has good sensitivity for glaucoma detection (Chauhan et al., 2013; Danthurebandara et al., 2016). In addition, longitudinal studies in the non-human primate suggest thinning of the NRR precedes that of RNFL thickness (Fortune et al., 2016a; He et al., 2014; Patel et al., 2014). In contrast to RNFL, the MRW thinned as pressure was increased, and a subsequent rebound was not seen when IOP was returned to 10 mmHg. The MRW thinning with increase in IOP was similar to that previously observed in both human and non-human primates (Ivers et al., 2016; Sharma et al., 2017; Strouthidis et al., 2011). In fact, when added to the deflection of the BMO height or Sclera-ALCS depth, the results correspond to those previously reported for the mean position of the disc (MPD) using other imaging methodologies (Burgoyne et al., 1995; Coleman et al., 1991; Heickell et al., 2001; Levy et al., 1981). In addition, studies where IOP was increased to 45 mmHg for 47 min and the eye imaged 2, 47, and 92 min after returning the IOP to 10 mmHg, the MPD did not return to baseline in 7 of the 10 normal eyes studied (Burgoyne et al., 1995), which in principal, correspond to the findings from the present study where the BMO height returns to baseline but the MRW does not.

The reduction of the NRR tissue thickness observed could be from; 1) axonal stretching, 2) a reduction in axonal diameter, 3) changes in the extracellular environment, 4) thinning of the glial columns or 5) compression of vasculature. Because there was not a significant change in the BMO-ALCS depth, it is unlikely that the MRW observation is from axonal stretching. It is also unlikely that MRW thinning is a result of vessel compression, as large changes in rim tissue thickness are noted in regions with or without major vasculature, and vascular data from OCTA do not correspond. In fact, we were unable to model realistic vessel density and caliber changes that would correspond to the thinning noted, as done for RNFL thickness. Additionally, based on previous studies in which IOP was elevated to 30 mmHg below mean arterial pressure and maintained for several hours, the axons of the prelaminar region had normal morphology (Quigley and Anderson, 1976). Although we are unable to ascertain the precise reason for MRW thinning, we hypothesize that it is a result of astrocyte compression and changes in the extracellular environment. Specifically, although glial cells have regional differences in elasticity, they have been shown to be ‘softer’ than neural cells (Lu et al., 2006; Lu et al., 2013). Overall, the thinning of the MRW with short-term changes in IOP as observed in this study are important to consider especially when using this metric to estimate RGC content in the eye as is done for structure function relationships. In addition, these findings support the hypothesis that IOP effects on the ONH NRR should be considered for glaucoma pathophysiology (Fortune et al., 2016b).

The vasculature of the ONH and surrounding tissue is often separated into regions supplied by the central retinal artery and by the posterior ciliary arteries. Specifically, the nerve fiber layer/radial peripapillary capillaries and superficial ONH tissue are supplied by branches of the central retinal artery, while the prelaminar tissue, lamina, and choroid are supplied by the posterior ciliaries (Cioffi and Van Buskirk, 1994; Hayreh, 1969; Henkind, 1969; Onda et al., 1995). OCTA algorithms allow for non-invasive imaging of ocular vasculature, and although blood velocity is typically not computed, vessels with active flow can be identified. Using OCTA, several investigators have shown either reduced flow or loss of radial peripapillary capillaries in glaucoma and glaucoma suspect patients (Akil et al., 2017; Chen et al., 2016; Lee et al., 2016; Rao et al., 2016; Yarmohammadi et al., 2016). In normal, healthy non-

human primate eyes, blood flow is known to have a transient decrease for ~4 seconds when IOP is increased up to 40 mmHg (Liang et al., 2010; Wang et al., 2014). In human subjects, using Doppler imaging, although systolic velocity is still present, diastolic velocity in the central retinal artery approaches 0 cm/s at approximately 45 mmHg (Guidoboni et al., 2014; Harris et al., 1996). In the present study, superficial vessels in each of the three annular zones showed a reduction in vessel density when the OPP decreased below 51.0±14.0mmHg within the BMO and 43.0±7.5mmHg for the immediate peripapillary annulus. In principal, these findings are in agreement with previous studies that have investigated blood flow as a function of IOP and MAP (Jiang et al., 2018; Wang et al., 2015; Zhi et al., 2015). While OPP in the present study included individual variability in MAP, the decrease in vessel density reached statistical significance only when IOP exceeded 50 mmHg, and quickly recovered when IOP dropped below 40 mmHg. Because capillaries as imaged with OCTA decrease in density only when IOP is relatively high, it may be sensitive to investigate if early changes in vessel density precede axonal loss in early experimental neuropathy. However, individual differences and short term fluctuations in MAP need to be taken into account.

An acute increase in IOP in human subjects has been shown to result in a decrease in choroid thickness (Song et al., 2016; Wang et al., 2016). In the current study, choroid thickness measured in 500 μm annular zones decreased with increase in IOP. Although there was an increase of thickness with reduction in IOP, only the BMO-500 μm annulus returned to baseline with lowering of IOP to 10 mmHg. Also, while thickness change increased with eccentricity from the BMO, the percentage change in thickness was greater closer to the BMO. While OCTA of deeper vasculature was not quantified, 500 μm slabs aligned to the top edge of the BM was used to objectively assess choroidal vasculature (Fig 12). Although there is significant variability between subjects, the visibility of choroidal vasculature improved with increase in IOP. We believe this increase in vessel appearance is likely a reflection of a loss of choriocapillaries signal and reduced shadowing from superficial and deep vascular plexus. In addition, with increase in IOP, there was loss of OCTA signal in the peripapillary region, which resembled choroidal microvascular dropout that has been reported in glaucoma patients with peripapillary zone beta atrophy (Lee et al., 2017; Suh et al., 2016). Along with changes in choroid, deeper slab angiography images show significant signal in the optic nerve head region. While this signal might represent vasculature in the lamina region, it is likely that it also includes projection artifacts from the superficial vasculature.

There are several limitations to this study. Although blood pressure was monitored for all subjects, there were differences between animals, and ideally, mean arterial pressure should have been kept constant across animals, and measured using an arterial line. Cannulation experiments have to be done on sedated animals, and the effects of anesthesia on ocular physiology cannot be completely accounted for. IOP was only allowed to equilibrate for 10 minutes prior to scanning the eye at each pressure setting. Even though significant changes were seen in morphology, because of the short duration of IOP stabilization at each setting, maximum change was not captured. All animals in this study were healthy, young adults, and age- or disease-associated differences could not be investigated.

In conclusion, the findings from this study demonstrate that there are differences in how the morphology of the ONH and surrounding tissues respond to IOP challenge. Specifically, while the BMO height and Sclera-ALCS measures were sensitive to each pressure increase, they also returned towards baseline when IOP was reduced. In contrast, OCTA vessel density only decreased at higher IOP levels, and returned to baseline as IOP was reduced, while the pressure-induced thinning of the MRW rebounded over a prolonged period of time. In addition, vessel compression could not completely account for the changes seen in either RNFL or MRW.

Supplementary Material

Refer to Web version on PubMed Central for supplementary material.

Acknowledgments

Research Support: K23 EY021761, R01 EY001139, T35 EY007088, P30 EY007551

References

Agoumi Y, Sharpe GP, Hutchison DM, Nicolela MT, Artes PH, Chauhan BC. Laminar and prelaminar tissue displacement during intraocular pressure elevation in glaucoma patients and healthy controls. Ophthalmology. 2011; 118:52–59. [PubMed: 20656352]

Akil H, Huang AS, Francis BA, Sadda SR, Chopra V. Retinal vessel density from optical coherence tomography angiography to differentiate early glaucoma, pre-perimetric glaucoma and normal eyes. PloS one. 2017; 12:e0170476. [PubMed: 28152070]

Anderson DR. Collaborative normal tension glaucoma study. Current opinion in ophthalmology. 2003; 14:86–90. [PubMed: 12698048]

Anderson DR, Hendrickson A. Effect of intraocular pressure on rapid axoplasmic transport in monkey optic nerve. Investigative ophthalmology. 1974; 13:771–783. [PubMed: 4137635]

Burgoyne CF. A biomechanical paradigm for axonal insult within the optic nerve head in aging and glaucoma. Exp Eye Res. 2011; 93:120–132. [PubMed: 20849846]

Burgoyne CF, Quigley HA, Thompson HW, Vitale S, Varma R. Measurement of optic disc compliance by digitized image analysis in the normal monkey eye. Ophthalmology. 1995; 102:1790–1799. [PubMed: 9098279]

Burgoyne CF, Varma R, Quigley HA, Vitale S, Pease ME, Lenane PL. Global and regional detection of induced optic disc change by digitized image analysis. Arch Ophthalmol. 1994; 112:261–268. [PubMed: 8311780]

Chauhan BC, O'Leary N, Almobarak FA, Reis AS, Yang H, Sharpe GP, Hutchison DM, Nicolela MT, Burgoyne CF. Enhanced detection of open-angle glaucoma with an anatomically accurate optical coherence tomography-derived neuroretinal rim parameter. Ophthalmology. 2013; 120:535–543. [PubMed: 23265804]

Chen CL, Zhang A, Bojikian KD, Wen JC, Zhang Q, Xin C, Mudumbai RC, Johnstone MA, Chen PP, Wang RK. Peripapillary Retinal Nerve Fiber Layer Vascular Microcirculation in Glaucoma Using Optical Coherence Tomography-Based Microangiography. Investigative ophthalmology & visual science. 2016 Oct.57:475–485.

Cioffi GA, Van Buskirk EM. Microvasculature of the anterior optic nerve. Surv Ophthalmol. 1994; 38(Suppl):S107–116. discussion S116–107. [PubMed: 7940132]

Coleman AL, Quigley HA, Vitale S, Dunkelberger G. Displacement of the optic nerve head by acute changes in intraocular pressure in monkey eyes. Ophthalmology. 1991; 98:35–40. [PubMed: 2023730]

Cull GA, Reynaud J, Wang L, Cioffi GA, Burgoyne CF, Fortune B. Relationship between orbital optic nerve axon counts and retinal nerve fiber layer thickness measured by spectral domain optical

coherence tomography. Investigative ophthalmology & visual science. 2012; 53:7766–7773. [PubMed: 23125332]

Danthurebandara VM, Vianna JR, Sharpe GP, Hutchison DM, Belliveau AC, Shuba LM, Nicolela MT, Chauhan BC. Diagnostic Accuracy of Glaucoma With Sector-Based and a New Total Profile-Based Analysis of Neuroretinal Rim and Retinal Nerve Fiber Layer Thickness. Investigative ophthalmology & visual science. 2016; 57:181–187. [PubMed: 26795824]

Downs JC. Optic nerve head biomechanics in aging and disease. Exp Eye Res. 2015; 133:19–29. [PubMed: 25819451]

Fazio MA, Johnstone JK, Smith B, Wang L, Girkin CA. Displacement of the Lamina Cribrosa in Response to Acute Intraocular Pressure Elevation in Normal Individuals of African and European Descent. Investigative ophthalmology & visual science. 2016; 57:3331–3339. [PubMed: 27367500]

Fortune B, Hardin C, Reynaud J, Cull G, Yang H, Wang L, Burgoyne CF. Comparing Optic Nerve Head Rim Width, Rim Area, and Peripapillary Retinal Nerve Fiber Layer Thickness to Axon Count in Experimental Glaucoma. Investigative ophthalmology & visual science. 2016a Oct. 57:404–412. [PubMed: 26848879]

Fortune B, Reynaud J, Hardin C, Wang L, Sigal IA, Burgoyne CF. Experimental Glaucoma Causes Optic Nerve Head Neural Rim Tissue Compression: A Potentially Important Mechanism of Axon Injury. Investigative ophthalmology & visual science. 2016b; 57:4403–4411. [PubMed: 27564522]

Fortune B, Reynaud J, Wang L, Burgoyne CF. Does optic nerve head surface topography change prior to loss of retinal nerve fiber layer thickness: a test of the site of injury hypothesis in experimental glaucoma. PloS one. 2013; 8:e77831. [PubMed: 24204989]

Fortune B, Yang H, Strouthidis NG, Cull GA, Grimm JL, Downs JC, Burgoyne CF. The effect of acute intraocular pressure elevation on peripapillary retinal thickness, retinal nerve fiber layer thickness, and retardance. Investigative ophthalmology & visual science. 2009; 50:4719–4726. [PubMed: 19420342]

Frangi, AF., Niessen, WJ., Vincken, KL., Viergever, MA. Multiscale vessel enhancement filtering. In: Wells, WM.Colchester, A., Delp, S., editors. Medical Image Computing and Computer-Assisted Intervention — MICCAI'98: First International Conference; Cambridge, MA, USA. October 11–13, 1998; Berlin, Heidelberg: Springer Berlin Heidelberg; 1998. p. 130-137.Proceedings

Girard MJ, Strouthidis NG, Ethier CR, Mari JM. Shadow removal and contrast enhancement in optical coherence tomography images of the human optic nerve head. Investigative ophthalmology & visual science. 2011; 52:7738–7748. [PubMed: 21551412]

Gordon MO, Beiser JA, Brandt JD, Heuer DK, Higginbotham EJ, Johnson CA, Keltner JL, Miller JP, Parrish RK 2nd, Wilson MR, Kass MA. The Ocular Hypertension Treatment Study: baseline factors that predict the onset of primary open-angle glaucoma. Arch Ophthalmol. 2002; 120:714–720. [PubMed: 12049575]

Guidoboni G, Harris A, Cassani S, Arciero J, Siesky B, Amireskandari A, Tobe L, Egan P, Januleviciene I, Park J. Intraocular pressure, blood pressure, and retinal blood flow autoregulation: a mathematical model to clarify their relationship and clinical relevance. Investigative ophthalmology & visual science. 2014; 55:4105–4118. [PubMed: 24876284]

Harris A, Joos K, Kay M, Evans D, Shetty R, Sponsel WE, Martin B. Acute IOP elevation with scleral suction: effects on retrobulbar haemodynamics. Br J Ophthalmol. 1996; 80:1055–1059. [PubMed: 9059269]

Hayreh SS. Blood supply of the optic nerve head and its role in optic atrophy, glaucoma, and oedema of the optic disc. Br J Ophthalmol. 1969; 53:721–748. [PubMed: 4982590]

He L, Yang H, Gardiner SK, Williams G, Hardin C, Strouthidis NG, Fortune B, Burgoyne CF. Longitudinal detection of optic nerve head changes by spectral domain optical coherence tomography in early experimental glaucoma. Investigative ophthalmology & visual science. 2014; 55:574–586. [PubMed: 24255047]

Heickell AG, Bellezza AJ, Thompson HW, Burgoyne CF. Optic disc surface compliance testing using confocal scanning laser tomography in the normal monkey eye. J Glaucoma. 2001; 10:369–382. [PubMed: 11711833]

Henkind P. Radial peripapillary capillaries of the retina. I. Anatomy: human and comparative. Br J Ophthalmol. 1967; 51:115–123. [PubMed: 4959937]

Henkind P. Microcirculation of the peripapillary retina. Transactions - American Academy of Ophthalmology and Otolaryngology. American Academy of Ophthalmology and Otolaryngology. 1969; 73:890–897.

Hood DC, Fortune B, Arthur SN, Xing D, Salant JA, Ritch R, Liebmann JM. Blood vessel contributions to retinal nerve fiber layer thickness profiles measured with optical coherence tomography. J Glaucoma. 2008; 17:519–528. [PubMed: 18854727]

Ivers KM, Yang H, Gardiner SK, Qin L, Reyes L, Fortune B, Burgoyne CF. In Vivo Detection of Laminar and Peripapillary Scleral Hypercompliance in Early Monkey Experimental Glaucoma. Investigative ophthalmology & visual science. 2016 Oct.57:388–403.

Jiang R, Xu L, Liu X, Chen JD, Jonas JB, Wang YX. Optic nerve head changes after short-term intraocular pressure elevation in acute primary angle-closure suspects. Ophthalmology. 2015; 122:730–737. [PubMed: 25556115]

Jiang X, Johnson E, Cepurna W, Lozano D, Men S, Wang RK, Morrison J. The effect of age on the response of retinal capillary filling to changes in intraocular pressure measured by optical coherence tomography angiography. Microvascular research. 2018; 115:12–19. [PubMed: 28782513]

Johnstone J, Fazio M, Rojananuangnit K, Smith B, Clark M, Downs C, Owsley C, Girard MJ, Mari JM, Girkin CA. Variation of the axial location of Bruch's membrane opening with age, choroidal thickness, and race. Investigative ophthalmology & visual science. 2014; 55:2004–2009. [PubMed: 24595390]

Lee EJ, Lee KM, Lee SH, Kim TW. OCT Angiography of the Peripapillary Retina in Primary Open-Angle Glaucoma. Investigative ophthalmology & visual science. 2016; 57:6265–6270. [PubMed: 27849312]

Lee EJ, Lee KM, Lee SH, Kim TW. Parapapillary Choroidal Microvasculature Dropout in Glaucoma: A Comparison between Optical Coherence Tomography Angiography and Indocyanine Green Angiography. Ophthalmology. 2017

Leske MC, Heijl A, Hyman L, Bengtsson B, Komaroff E. Factors for progression and glaucoma treatment: the Early Manifest Glaucoma Trial. Current opinion in ophthalmology. 2004; 15:102–106. [PubMed: 15021220]

Levy NS, Crapps EE. Displacement of optic nerve head in response to short-term intraocular pressure elevation in human eyes. Arch Ophthalmol. 1984; 102:782–786. [PubMed: 6721773]

Levy NS, Crapps EE, Bonney RC. Displacement of the optic nerve head. Response to acute intraocular pressure elevation in primate eyes. Arch Ophthalmol. 1981; 99:2166–2174. [PubMed: 7305717]

Liang Y, Fortune B, Cull G, Cioffi GA, Wang L. Quantification of dynamic blood flow autoregulation in optic nerve head of rhesus monkeys. Exp Eye Res. 2010; 90:203–209. [PubMed: 19853603]

Lu YB, Franze K, Seifert G, Steinhauser C, Kirchhoff F, Wolburg H, Guck J, Janmey P, Wei EQ, Kas J, Reichenbach A. Viscoelastic properties of individual glial cells and neurons in the CNS. Proceedings of the National Academy of Sciences of the United States of America. 2006; 103:17759–17764. [PubMed: 17093050]

Lu YB, Pannicke T, Wei EQ, Bringmann A, Wiedemann P, Habermann G, Buse E, Kas JA, Reichenbach A. Biomechanical properties of retinal glial cells: comparative and developmental data. Exp Eye Res. 2013; 113:60–65. [PubMed: 23712083]

Morgan WH, Chauhan BC, Yu DY, Cringle SJ, Alder VA, House PH. Optic disc movement with variations in intraocular and cerebrospinal fluid pressure. Investigative ophthalmology & visual science. 2002; 43:3236–3242. [PubMed: 12356830]

Musial G, Rajagopalan LP, Patel NB, Schill AW, Queener HM, Adhikari S, Porter J. Longitudinal repeatability of imaging perfused retinal capillaries in normal human and non-human primate eyes using adaptive optics. Investigative ophthalmology & visual science. 2017; 58:315–315.

Onda E, Cioffi GA, Bacon DR, Van Buskirk EM. Microvasculature of the human optic nerve. Am J Ophthalmol. 1995; 120:92–102. [PubMed: 7611333]

Patel NB, Hung LF, Harwerth RS. Postnatal maturation of the fovea in Macaca mulatta using optical coherence tomography. Exp Eye Res. 2017; 164:8–21. [PubMed: 28778401]

Patel NB, Luo X, Wheat JL, Harwerth RS. Retinal nerve fiber layer assessment: area versus thickness measurements from elliptical scans centered on the optic nerve. Investigative ophthalmology & visual science. 2011; 52:2477–2489. [PubMed: 21220552]

Patel NB, Sullivan-Mee M, Harwerth RS. The relationship between retinal nerve fiber layer thickness and optic nerve head neuroretinal rim tissue in glaucoma. Investigative ophthalmology & visual science. 2014; 55:6802–6816. [PubMed: 25249610]

Patel, NB., Wheat, JXL., Harwerth, R. Optom Vis Sci. American Academy of Optometry; San Francisco: 2010. Retinal Vasculature and Retinal Nerve Fiber Layer Brightness in Normal and Glaucoma Eyes.

Qiao-Grider Y, Hung LF, Kee CS, Ramamirtham R, Smith EL 3rd. Normal ocular development in young rhesus monkeys (Macaca mulatta). Vision Res. 2007; 47:1424–1444. [PubMed: 17416396]

Quigley H, Anderson DR. The dynamics and location of axonal transport blockade by acute intraocular pressure elevation in primate optic nerve. Investigative ophthalmology. 1976; 15:606–616. [PubMed: 60300]

Quigley HA, Addicks EM. Chronic experimental glaucoma in primates. II. Effect of extended intraocular pressure elevation on optic nerve head and axonal transport. Investigative ophthalmology & visual science. 1980; 19:137–152. [PubMed: 6153173]

Quigley HA, Anderson DR. Distribution of axonal transport blockade by acute intraocular pressure elevation in the primate optic nerve head. Investigative ophthalmology & visual science. 1977; 16:640–644. [PubMed: 68942]

Quigley HA, Pease ME. Change in the optic disc and nerve fiber layer estimated with the glaucoma-scope in monkey eyes. J Glaucoma. 1996; 5:106–116. [PubMed: 8795742]

Rao HL, Kadambi SV, Weinreb RN, Puttaiah NK, Pradhan ZS, Rao DA, Kumar RS, Webers CA, Shetty R. Diagnostic ability of peripapillary vessel density measurements of optical coherence tomography angiography in primary open-angle and angle-closure glaucoma. Br J Ophthalmol. 2016

Scoles D, Gray DC, Hunter JJ, Wolfe R, Gee BP, Geng Y, Masella BD, Libby RT, Russell S, Williams DR, Merigan WH. In-vivo imaging of retinal nerve fiber layer vasculature: imaging histology comparison. BMC ophthalmology. 2009; 9:9. [PubMed: 19698151]

Sharma S, Tun TA, Baskaran M, Atalay E, Thakku SG, Liang Z, Milea D, Strouthidis NG, Aung T, Girard MJ. Effect of acute intraocular pressure elevation on the minimum rim width in normal, ocular hypertensive and glaucoma eyes. Br J Ophthalmol. 2017

Sigal IA, Grimm JL, Schuman JS, Kagemann L, Ishikawa H, Wollstein G. A method to estimate biomechanics and mechanical properties of optic nerve head tissues from parameters measurable using optical coherence tomography. IEEE transactions on medical imaging. 2014; 33:1381–1389. [PubMed: 24691117]

Sigal IA, Yang H, Roberts MD, Burgoyne CF, Downs JC. IOP-induced lamina cribrosa displacement and scleral canal expansion: an analysis of factor interactions using parameterized eye-specific models. Investigative ophthalmology & visual science. 2011; 52:1896–1907. [PubMed: 20881292]

Song W, Huang P, Dong X, Li X, Zhang C. Choroidal Thickness Decreased in Acute Primary Angle Closure Attacks with Elevated Intraocular Pressure. Curr Eye Res. 2016; 41:526–531. [PubMed: 26079201]

Strouthidis NG, Fortune B, Yang H, Sigal IA, Burgoyne CF. Effect of acute intraocular pressure elevation on the monkey optic nerve head as detected by spectral domain optical coherence tomography. Investigative ophthalmology & visual science. 2011; 52:9431–9437. [PubMed: 22058335]

Suh MH, Zangwill LM, Manalastas PI, Belghith A, Yarmohammadi A, Medeiros FA, Diniz-Filho A, Saunders LJ, Weinreb RN. Deep Retinal Layer Microvasculature Dropout Detected by the Optical Coherence Tomography Angiography in Glaucoma. Ophthalmology. 2016; 123:2509–2518. [PubMed: 27769587]

Wang L, Cull G, Burgoyne CF, Thompson S, Fortune B. Longitudinal alterations in the dynamic autoregulation of optic nerve head blood flow revealed in experimental glaucoma. Investigative ophthalmology & visual science. 2014; 55:3509–3516. [PubMed: 24812551]

Wang L, Cull GA, Fortune B. Optic nerve head blood flow response to reduced ocular perfusion pressure by alteration of either the blood pressure or intraocular pressure. Curr Eye Res. 2015; 40:359–367. [PubMed: 24911311]

Wang YX, Jiang R, Ren XL, Chen JD, Shi HL, Xu L, Wei WB, Jonas JB. Intraocular pressure elevation and choroidal thinning. Br J Ophthalmol. 2016; 100:1676–1681. [PubMed: 27016503]

Yang H, Downs JC, Sigal IA, Roberts MD, Thompson H, Burgoyne CF. Deformation of the normal monkey optic nerve head connective tissue after acute IOP elevation within 3-D histomorphometric reconstructions. Investigative ophthalmology & visual science. 2009; 50:5785–5799. [PubMed: 19628739]

Yarmohammadi A, Zangwill LM, Diniz-Filho A, Suh MH, Manalastas PI, Fatehee N, Yousefi S, Belghith A, Saunders LJ, Medeiros FA, Huang D, Weinreb RN. Optical Coherence Tomography Angiography Vessel Density in Healthy, Glaucoma Suspect, and Glaucoma Eyes. Investigative ophthalmology & visual science. 2016 Oct.57:451–459.

Yu PK, Cringle SJ, Yu DY. Correlation between the radial peripapillary capillaries and the retinal nerve fibre layer in the normal human retina. Exp Eye Res. 2014; 129:83–92. [PubMed: 25447563]

Zhi Z, Cepurna W, Johnson E, Jayaram H, Morrison J, Wang RK. Evaluation of the effect of elevated intraocular pressure and reduced ocular perfusion pressure on retinal capillary bed filling and total retinal blood flow in rats by OMAG/OCT. Microvascular research. 2015; 101:86–95. [PubMed: 26186381]

Highlights

- There are differences in how the tissues of the optic nerve head (ONH) and cicumpapillary tissue respond to gradient increases and decreases in IOP.
- Optical coherence tomography vessel density decreases gradually, reaching statistical significance only when IOP is greater than 50 mmHg, but returns to baseline when IOP is decreased.
- The ONH minimum rim width decreases with increase in IOP and does not return to baseline when IOP is reduced.
- There is no significant change in the peripapillary RNFL thickness with acute IOP increase, followed by return.
- Changes in vessel density were not related to those of RNFL or MRW.

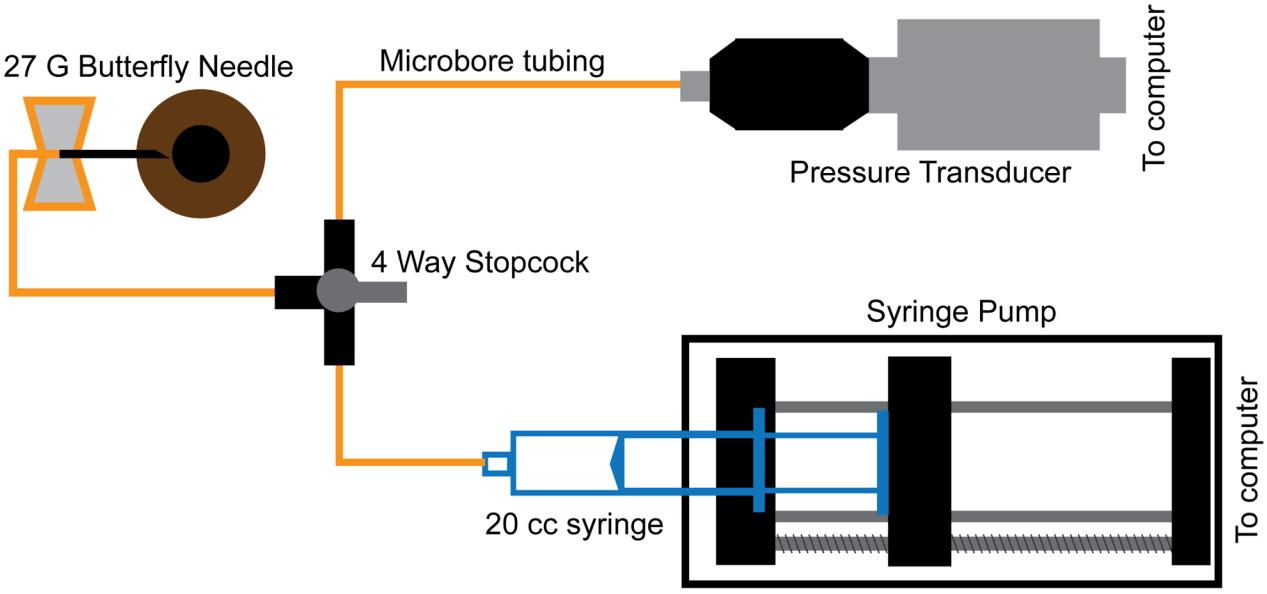

Figure 1.
Components and setup used for IOP control.

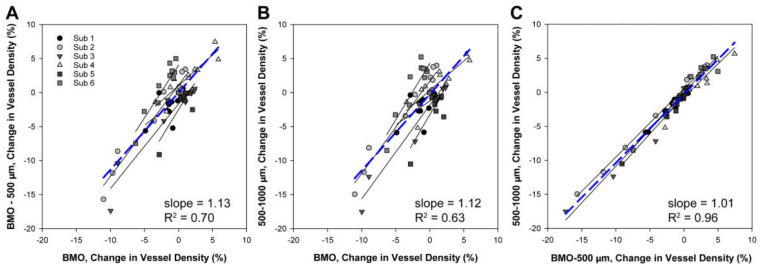

Figure 2.

A. 20° IR-SLO image with BMO points (yellow markers) and best fit ellipse (red). The green ellipse illustrates the scan path for the B-scan used for RNFL analysis in B. Interpolated B-scan with RNFL borders segmented. RNFL thickness was calculated after removing major retinal vasculature (blue). C. 20° IR-SLO image with 24 line radial scan D. 30° IR-SLO image with choroid thickness map. The green, yellow and blue ellipses correspond to eccentricities from the BMO of 500µm, 1000µm, and 1500µm. E. Enhanced horizontal radial b-scan (red line in C) through the ONH illustrating the segmentation for ILM, BM, choroid, and lamina, and reference points for the BMO and 4mm plane.

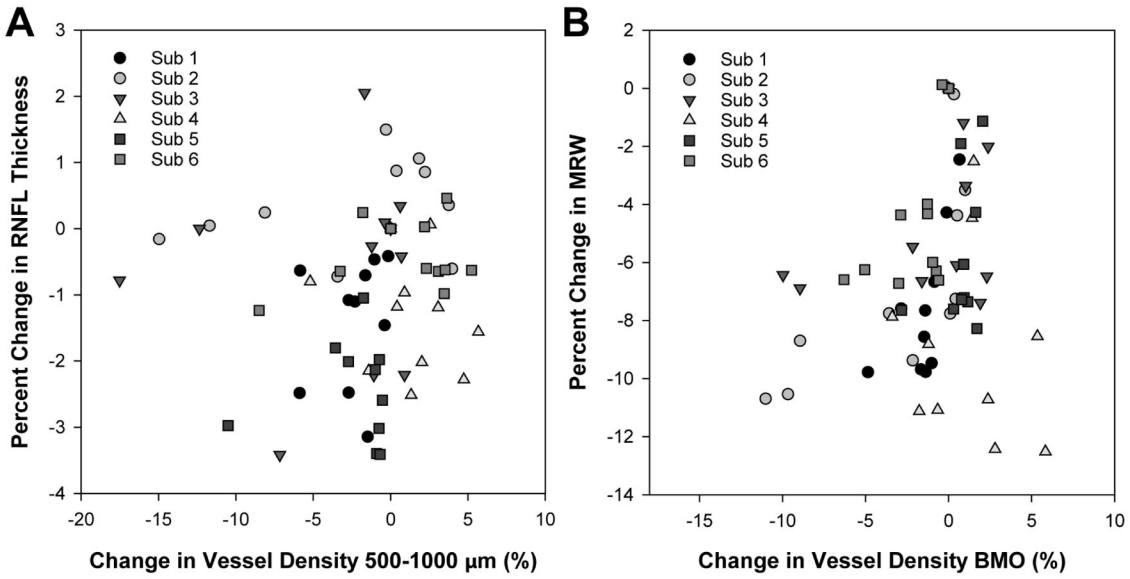

Figure 3.

A. 20° OCT b-scan illustrating the three reference planes used; 1) BMO, 2) 4mm diameter plane aligned to the BM and centered on the BMO, and 3) 4mm diameter plane aligned to the choroid/sclera junction and centered on the BMO. B. SLO image with BMO points indicated (red). The green points correspond to locations on radial b-scans where the lamina was visible and marked on radial b-scans. C. Spline surface fit to the lamina points marked in B, and confined to the BMO.

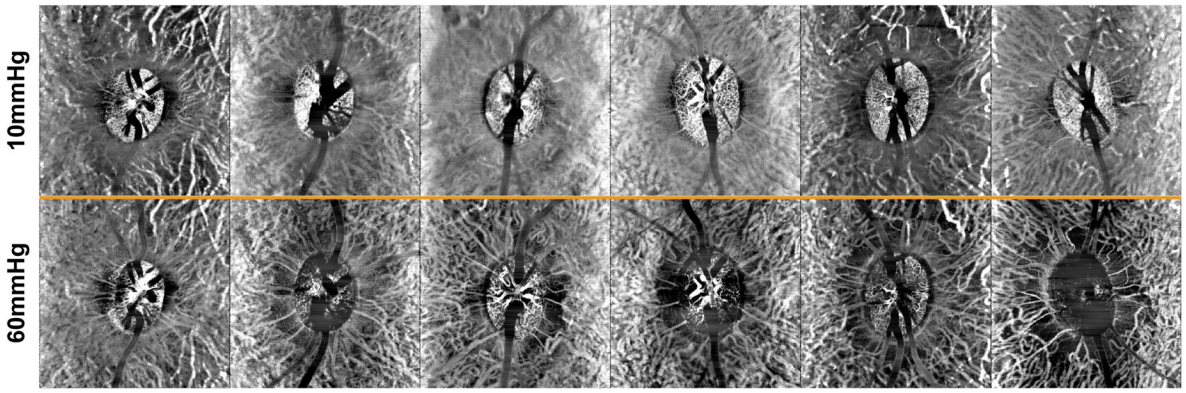

Figure 4.

A 20° SLO image with 15×15° OCT angiography slab, 150 μm thick, referenced to the ILM. B. OCT angiography slab following accentuation using a Frangi filter. C. Threshold image used for calculating vessel density. D. The three ellipses correspond to the best fit to the BMO, an eccentricity of 500 μm from the BMO, and an eccentricity of 1000 μm from the BMO.

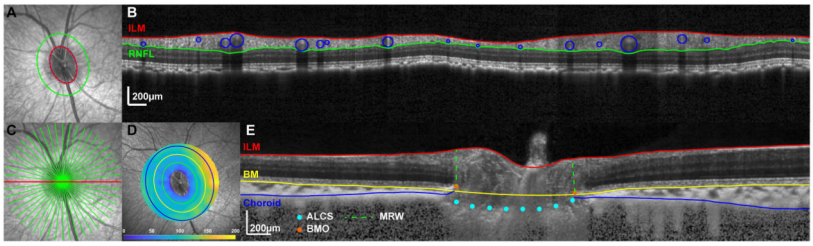

Figure 5.

The plots illustrate the mean difference ± standard error from the initial 10mmHg IOP setting for ONH structural features. Measures from the ascending IOP phase were compared to that at 10mmHg, and a statistically significant difference is noted by an *. Measures from the descending IOP phase were compared to those at 60mmHg and statistically significant differences are noted by †. A difference in the two 10mmHg measures is marked with ‡

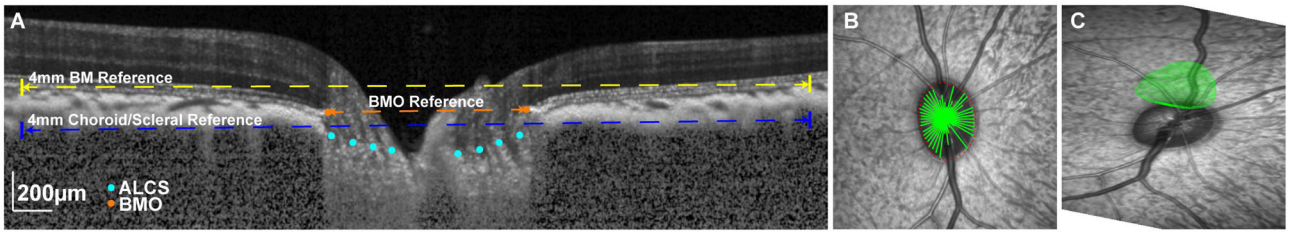

Figure 6.

The plots illustrate the mean difference ± standard error from the initial 10mmHg IOP setting for vascular (choroid and OCTA) features. Measures from the ascending IOP phase were compared to that at 10mmHg, and a statistically significant difference is noted by an *. Measures from the descending IOP phase were compared to those at 60mmHg and statistically significant differences are noted by †. A difference in the two 10mmHg measures is marked with ‡

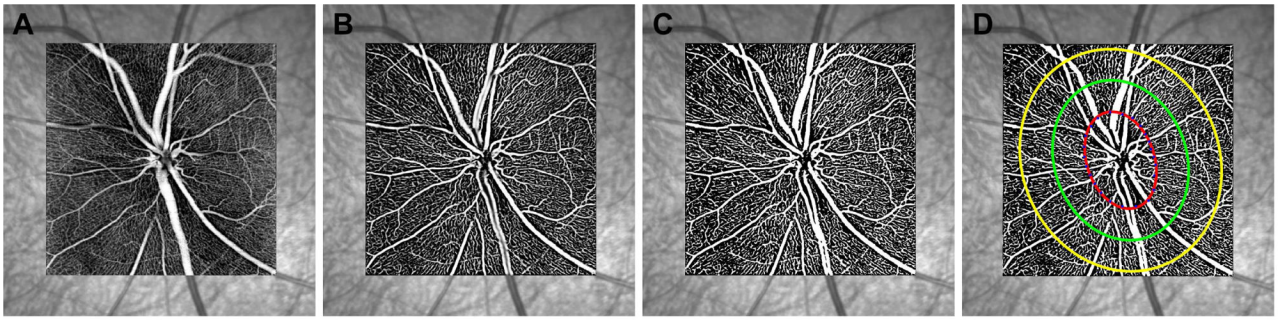

Figure 7.

Relationship of normalized change in choroid thickness for the three annular zones. Each subject is represented by a different shape and shade of gray. The solid line fits are for individual animals, and the dashed blue line represents the best fit for the grouped data.

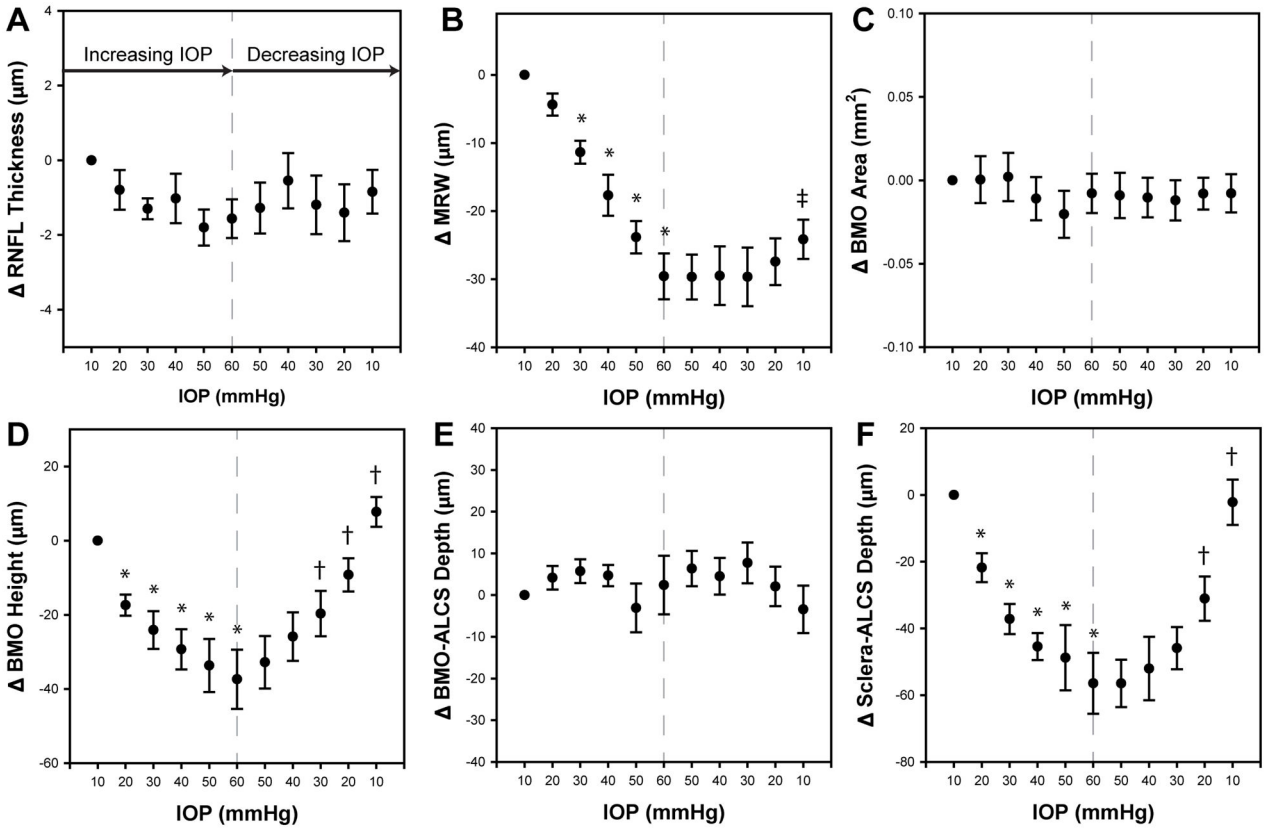

Figure 8.

The top row illustrates a 150 μm OCT angiography slab aligned to the ILM at 10mmHg for all animals. The bottom row are identical slabs at 60mmHg pressures.

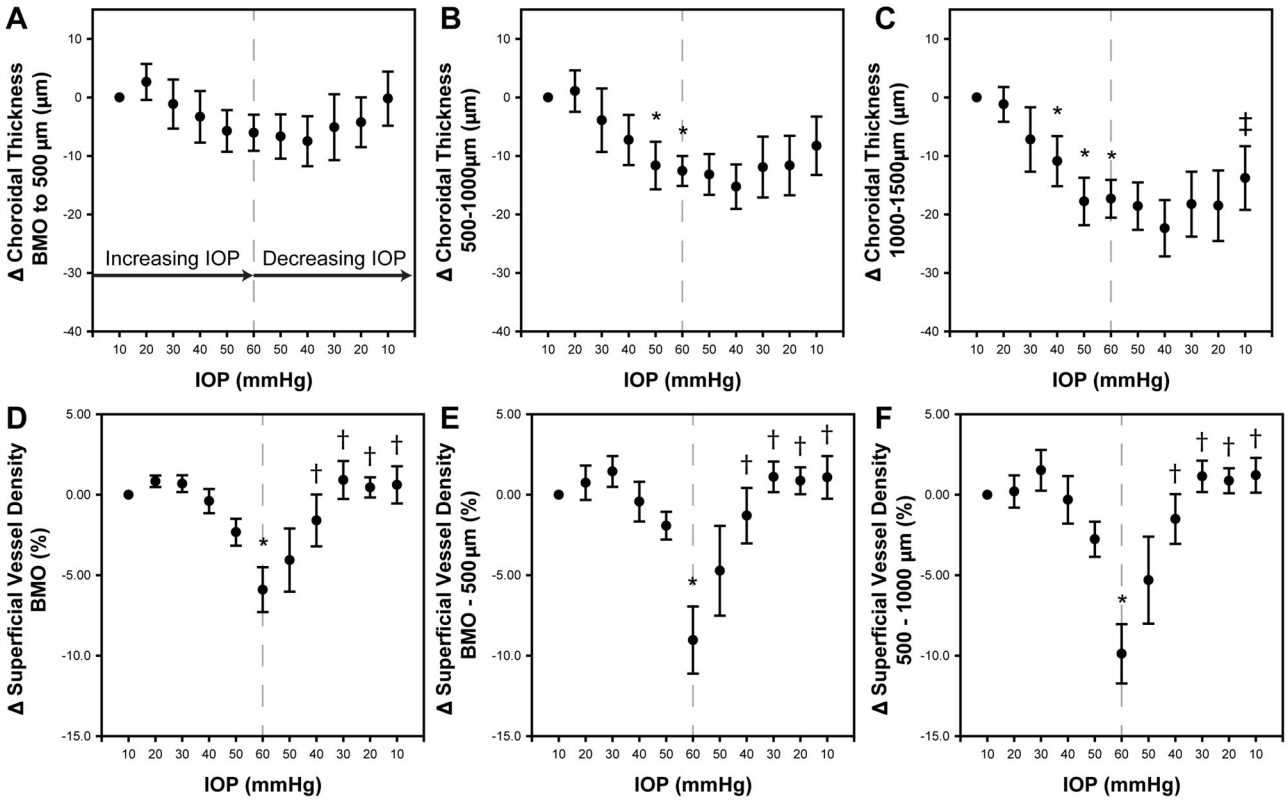

Figure 9.

Relationship between ocular perfusion pressure and vessel density for the three annular zones. Each subject is represented by a different shape and shade of gray.

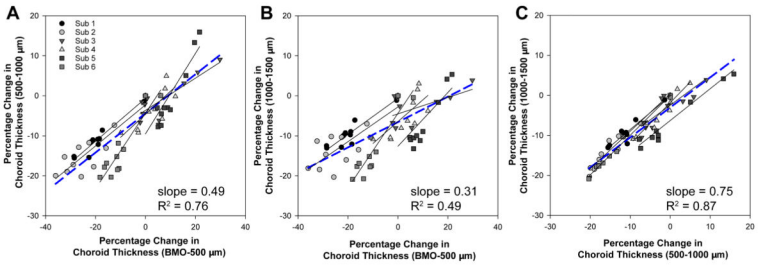

Figure 10.

Relationship of change in vessel density for the three annular zones. Each subject is represented by a different shape and shade of gray. The solid line fits are for individual animals, and the dashed blue line represents the best fit for the grouped data.

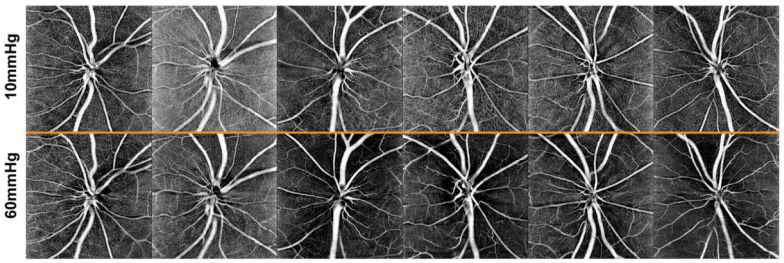

Figure 11.

A. Scatterplot illustrating percentage change in RNFL thickness as a function of change in vessel density in the same region. B. Scatterplot illustrating percentage change in MRW as a function of change in vessel density in the region of the BMO.

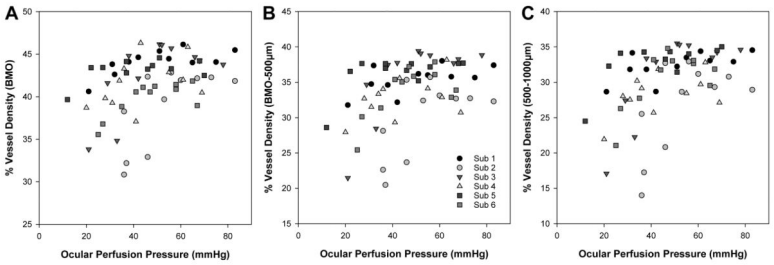

Figure 12.

The top row illustrates a 500 μm OCT angiography slab aligned to the BM at 10mmHg for all animals. The bottom row are identical slabs at 60mmHg pressures.

Table 1

Age, and biometric measures of the six subjects prior to anterior chamber cannulation. The mean arterial pressure median and range is for the duration of the imaging experiments.

Subject	Age (years)	Corneal Curvature (D)	Central Corneal Thickness (μm)	Lens Thickness (mm)	Axial Length (mm)	Anterior Chamber Depth (mm)	Mean Arterial Pressure (mmHg), median and range
Sub 1	4.1	50.65	443	3.53	19.68	3.38	89 (85 – 100)
Sub 2	5.3	55.06	419	3.33	17.68	3.30	93 (87 – 110)
Sub 3	5.2	53.10	460	3.38	19.52	3.70	88 (83 – 95)
Sub 4	5.2	55.43	447	3.52	18.37	3.57	85 (71 – 88)
Sub 5	5.1	55.64	477	3.31	19.10	3.71	84 (78 – 87)
Sub 6	6.3	49.57	472	3.23	19.48	3.46	85 (82 – 92)

Table 2

Mean and standard deviations for all measures quantified, at each pressure setting. The repeated measures ANOVA for each measure is illustrated in the last column.

	ASCENDING PRESSURE (mmHg)						DECENDING PRESSURE (mmHg)					RMANOVA, F(10,50), p
	10	**20**	**30**	**40**	**50**	**60**	**50**	**40**	**30**	**20**	**10**	
BMO Area (mm^2)	1.19 (0.10)	1.19 (0.12)	1.19 (0.13)	1.18 (0.12)	1.17 (0.11)	1.18 (0.11)	1.18 (0.12)	1.18 (0.12)	1.18 (0.12)	1.18 (0.11)	1.18 (0.12)	1.23, 0.30
BMO Height (μm)	73.08 (28.21)	90.47 (31.37)	97.20 (32.62)	102.40 (34.26)	106.76 (35.30)	110.78 (35.15)	105.90 (33.48)	98.97 (32.46)	92.74 (30.20)	82.30 (26.40)	65.32 (20.85)	15.86, <0.01
BMO-ALCS Depth (μm)	153.48 (36.51)	157.65 (40.27)	159.22 (38.65)	158.17 (36.82)	150.40 (36.64)	155.89 (33.67)	159.85 (34.16)	158.00 (37.43)	161.21 (38.79)	155.55 (32.80)	150.06 (29.64)	1.56, 0.15
Sclera-ALCS Depth (μm)	72.56 (35.71)	94.31 (35.92)	109.74(31.38)	118.01 (34.29)	121.34 (34.89)	129.01 (34.58)	129.02 (39.0)	124.60 (42.6)	118.46 (37.3)	103.61 (38.44)	74.73 (36.23)	22.02, <0.01
MRW (μm)	341.64 (47.46)	337.29 (45.41)	330.30 (46.91)	323.97 (44.26)	317.81 (44.35)	312.07 (44.37)	311.97 (44.17)	312.15 (41.85)	311.98 (42.28)	314.21 (41.30)	317.49 (43.09)	46.29, <0.01
RNFL Thickness (μm)	114.27 (5.12)	113.48 (5.20)	112.97 (4.92)	113.25 (4.69)	112.47 (5.14)	112.71 (5.33)	113.00 (5.55)	113.73 (4.83)	113.08 (4.35)	112.87 (4.56)	113.43 (4.62)	1.24, 0.29
Choroid BMO-500 (μm)	63.73 (12.11)	66.39 (16.71)	62.60 (18.26)	60.43 (17.62)	58.02 (15.41)	57.70 (12.96)	57.07 (15.06)	56.26 (15.39)	58.65 (17.35)	59.49 (15.00)	63.54 (15.42)	3.04, <0.01
Choroid 500–1000 (μm)	112.75 (25.63)	113.84 (24.39)	108.85 (23.57)	105.48 (22.48)	101.13 (19.93)	100.20 (21.72)	99.59 (20.23)	97.50 (19.45)	100.84 (17.75)	101.11 (18.51)	104.49 (18.08)	6.72, <0.01
Choroid 1000–1500 (μm)	148.69 (37.97)	147.52 (33.95)	141.51 (29.28)	137.81 (31.49)	130.91 (29.24)	131.37 (32.21)	130.11 (31.42)	126.33 (27.53)	130.44 (26.43)	130.19 (25.37)	134.92 (26.82)	10.18, <0.01
Vessel Density BMO (%)	42.7 (1.7)	43.5 (1.9)	43.3 (2.11)	42.3 (3.0)	40.3 (2.6)	36.8 (3.4)	38.6 (5.0)	41.1 (4.1)	43.6 (2.7)	43.1 (1.7)	43.3 (2.4)	5.98, <0.01
Vessel Density BMO-500 (%)	35.0 (3.4)	35.7 (2.5)	36.4 (2.0)	34.6 (3.2)	33.1 (3.7)	25.9 (4.4)	30.3 (7.4)	33.7 (5.1)	36.1 (2.2)	35.9 (2.0)	36.1 (2.4)	6.96, <0.01
Vessel Density 500–1000 (%)	31.6 (3.5)	31.8 (2.0)	33.1 (1.9)	31.3 (3.4)	28.9 (3.5)	21.8 (4.4)	26.3 (7.3)	30.1 (4.9)	32.8 (2.3)	32.5 (2.4)	32.8 (1.4)	8.25, <0.01